The impact of vacancies on the stability of cubic phases in Sb–Te binary compounds

Xin Chen[1,2,3], Xianqiang Liu[2], Yan Cheng[1,4] and Zhitang Song[1]

Abstract

Data retention ability and number of cycles are key properties of phase change materials in applications. Combining in situ heating transmission electron microscopy with ab initial calculations, we investigated the phase transitions of binary Sb–Te compounds. The calculations indicated that the vacancies in Te sites destroyed the framework of the cubic phase, which agrees well with the absence of cubic phases observed during in situ heating experiments when the Sb concentration exceeded 50%. In contrast, the vacancies in Sb sites stabilized the cubic structure. Further analysis of the charge density maps revealed that the distribution of antibonding electrons may be the origin of the driving force for structural transitions. Furthermore, our results also showed that reducing the vacancies greatly increased the phase transition temperatures of both the amorphous-cubic and cubic-trigonal phases and therefore may improve the data retention ability and cyclability of phase change materials. This result also implies that doping Sb–Te compounds may provide an approach to discover novel phase change materials by reducing the amount of vacancies.

Introduction

Recent major breakthroughs that addressed the limitations[1] of phase change memory (PCM) are renewing interest in it as a promising next-generation technology for electronic data storage and computation[2,3]. If the performance of PCM could compete with that of dynamic random access memory (DRAM), completely new computer architectures would be enabled[4]. To date, the most widely studied systems lie on, or are in the vicinity of, a pseudobinary line that joins the stoichiometric compounds Sb_2Te_3 and GeTe. Among these compounds, the alloy $Ge_2Sb_2Te_5$ has the best combination of properties: fast crystallization, amorphous phase stability, high endurance limit and excellent contrast;[5] therefore, it has attracted the largest amount of attention. The crystalline phase utilized in GeSbTe-based PCMs that are currently in use is the cubic metastable phase, which contains large quantities of vacancies[6–8]. The vacancies in the Ge/Sb sublattice are intrinsic[9] and have been demonstrated to play an important role in phase transitions and related properties[10–17].

Replacing DRAM with PCM is a formidable challenge because of the combined requirements of a fast switching speed and extremely high cycle numbers. Although a Sb-rich GeSbTe PCM demonstrated 10^{11} cycles under accelerated testing conditions[18], the required cycle numbers for a DRAM replacement have not been achieved[4]. One of the main failure mechanisms of PCM devices is void formation over the bottom electrode contact. The other main failure mechanism is elemental segregation, which leads to poor data retention when the cell can no longer be switched to the high-resistance state or does not remain in the high-resistance state since Sb-rich alloys have low crystallization temperatures[4].

In terms of the failure mechanism in GeSbTe-based PCMs, Sb–Te alloys have advantages compared to GeSbTe alloys, e.g., a simple composition, which prevents the phase separation that occurs in GeSbTe alloys. As the parent material of GeSbTe PCMs, Sb_2Te_3 and its promise

Correspondence: Xianqiang Liu (xqliu@bjut.edu.cn) or
Zhitang Song (ztsong@mail.sim.ac.cn)
[1]State Key Laboratory of Functional Materials for Informatics, Shanghai Institute of Micro-system and Information Technology, Chinese Academy of Sciences, 200050 Shanghai, China
[2]Institute of Microstructure and Property of Advanced Materials, Beijing University of Technology, 100124 Beijing, China
Full list of author information is available at the end of the article.

have been ignored for a substantial amount of time. Recently, Zheng et al. proved that the metastable face-centered cubic (FCC) Sb_2Te_3 phase does exist[8]. A series of studies showed that-doped Sb_2Te_3 exhibits excellent properties that are required for PCMs[19,20], such as a fast phase transition speed, good reversibility at elevated temperatures and good thermal stability at room temperature. In 2017, Rao et al. demonstrated that the $Sc_{0.2}Sb_2Te_3$ compound that they designed achieved a writing speed of only 700 picoseconds[7]. The ultrafast crystallization is due to the reduced stochasticity of nucleation through geometrically matched and robust scandium telluride (ScTe) chemical bonds that stabilize the crystal precursors in the amorphous state. This makes Sb_2Te_3 an attractive competitor to DRAM because of the ultrafast writing speed. Unfortunately, as a DRAM replacement, Sb_2Te_3 possesses the same shortcomings as GeSbTe. Due to the large quantities of volatile vacancies in the metastable phase, the cubic phase has a strong tendency to transform into a stable trigonal phase during cyclic writing processes. The vacancy ordering and evaporation from the cubic phase to the trigonal phase result in a density change[21], which causes void formation, triggering the failure of PCMs[4]. Additionally, pure Sb_2Te_3 has a very low crystallization temperature and thus a poor data retention ability.

Here, in this work, we systematically investigated the phase transitions of Sb–Te binary compounds between Sb_2Te_3 and Sb_2Te by combining in situ heating transmission electron microscopy (TEM) and ab initio calculations. The in situ TEM experiments showed that vacancies play a central role in the phase transition temperatures of Sb–Te compounds. The ab initio calculations revealed that the vacancy type is the factor that determines the existence of a cubic phase and that the amount of vacancies has a great impact on the phase transition temperatures.

Materials and methods

Film preparation and characterization

The TEM samples (~15 nm) were deposited on copper grids with an ultrathin carbon support by varying the RF sputtering power on Sb and Sb_2Te_3 targets by physical vapor deposition (PVD). The deposition rate was measured from cross-section samples by scanning electron microscopy (SEM). The sample composition was tested by energy dispersive spectroscopy (EDS) (shown in Supplementary Fig. 10). The in situ heating experiments were performed with TEM (JEOL 2100F) with a heating rate of 10 °C/min using a single tilt holder (Gatan 628). To alleviate the influence of electron irradiation, the samples were exposed to the beam for a short time at the capturing temperature, and the area was changed for each observation. High-resolution TEM (HRTEM) experiments were performed on a JEOL-ARM300F instrument with a double Cs corrector operating at 300 kV.

Ab initio theoretical simulation

The ab initio calculations were carried out by employing the Vienna ab initio simulation package (VASP)[22] with projected augmented wave (PAW) pseudopotentials[23] and Perdew-Burke-Ernzerhof (PBE) functionals[24]. The $14.942 \times 14.942 \times 31.697$ (Å) supercell of the FCC structure was built. For the stable structures with a trigonal phase with van der Waals (vdW) gaps, the DFT-D2 method of the Grimme scheme[25] was used for corrections. The energy cut-off was set to 235 eV, and the Γ point was used in the Brillouin zone sum. Chemical bonding analysis was carried out by combining a charge density map with the COHP method[26]. The Local Orbital Basis Suite Towards Electronic-Structure Reconstruction (LOBSTER) code[27] handles the DFT calculation results and projects them onto localized atomic basis sets[28]. The activation energies of the atom/vacancy diffusion were calculated using the nudged elastic band (NEB) method[29,30].

Fig. 1 The electron diffraction profiles showing the structure evolutions of Sb-Te binary compounds in in-situ TEM heating experiments. a Intensity profiles extracted from diffraction rings at an elevated temperature for different Sb concentrations. **b** The temperature of the different phase changes with the variation in the Sb concentration. Blue represents the amorphous phase (A), green represents the FCC phase (F) and red represents the trigonal phase (T)

Results and discussion

In situ TEM characterization of the phase transformations of Sb–Te compounds

Figure 1a shows an intensity profile extracted from the diffraction patterns (Supplementary Figs 1–4) of in situ heating experiments for Sb–Te compounds with different Sb concentrations. In Fig. 1a, the intensity profiles of the diffraction patterns indicate that partial Sb_2Te_3 films crystallized even at room temperature. Some crystalline grains (below 10 nm) were found in the TEM bright-field (BF) image (Supplementary Fig. 1). The indexed diffraction pattern shows that the structure at room temperature belonged to the FCC phase. With increasing temperature,

an increasing number of large grains (~10 nm) appeared. The intensity profiles of the diffraction patterns indicated that up to 120 °C, the crystals retained the cubic structure. At 140 °C, the 2Θ value of the (200) FCC peak decreased, indicating that the phase changed to a trigonal structure.

When the composition approached SbTe ($Sb_{48}Te_{52}$), the intensity profile of the as-deposited film was characterized as an amorphous phase. Although some grain-like particles appeared in the BF image at 100 °C (Supplementary Fig. 2), the cubic phase did not appear in the intensity profile until 120 °C and remained until 200 °C. At 200 °C, the (222) peak of the cubic phase shifted slightly to the left, indicating incubation of the trigonal
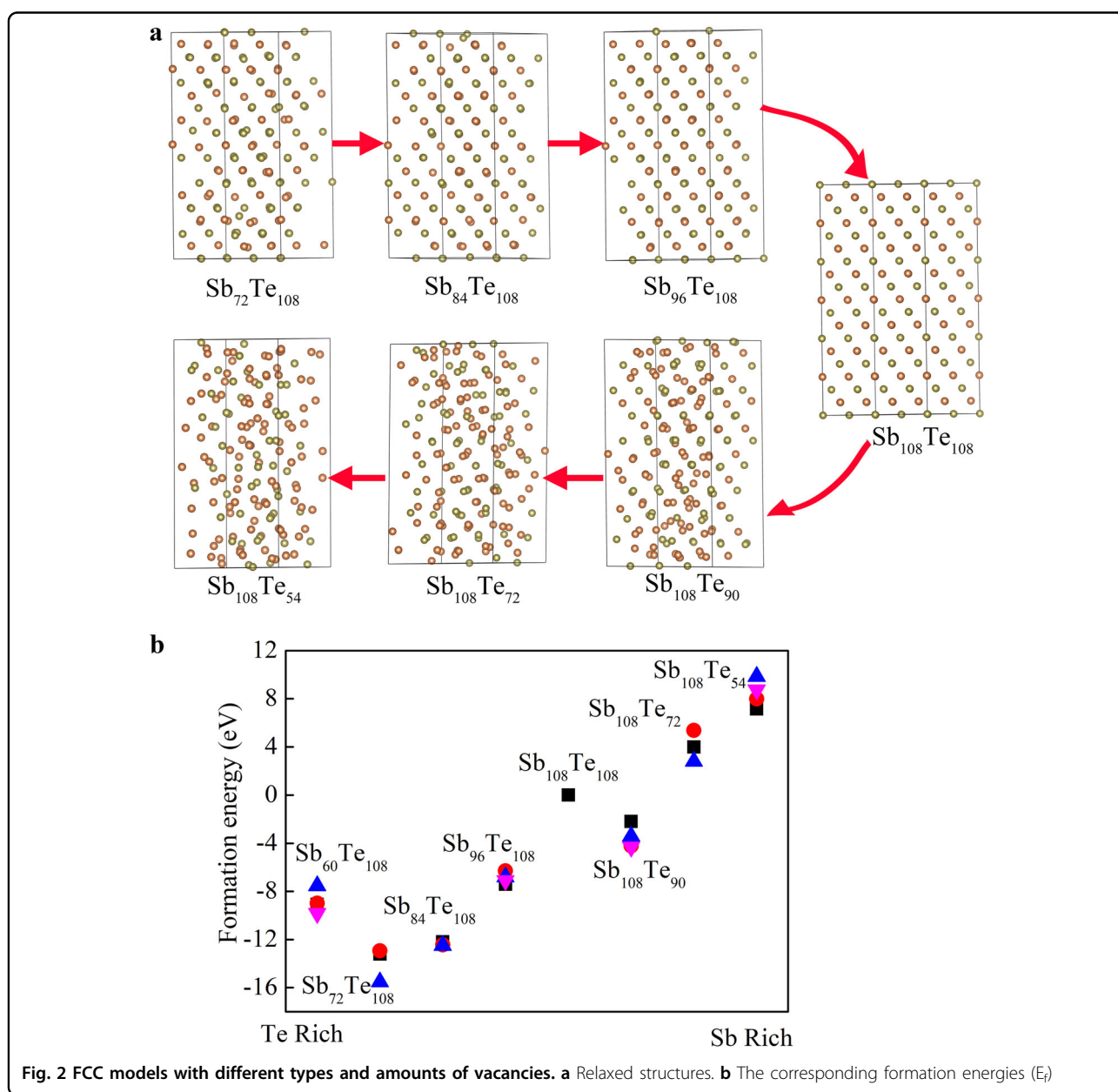
Fig. 2 FCC models with different types and amounts of vacancies. a Relaxed structures. **b** The corresponding formation energies (E_f)

phase. When the temperature increased to 220 °C, the intensity profile showed a well-characterized trigonal phase. To confirm the structure of the $Sb_{48}Te_{52}$, HRTEM was performed to observe the image of the film after heating to 160 °C (Supplementary Fig. 5). The HRTEM images of the < 0 0 1 >, < 1 1 1 > and < 1 1 0 > zone axes clearly indicate the existence of the FCC phase, which is quite similar to cubic Sb_2Te_3[8]. However, when the composition crossed the SbTe line, the phase transition of the compound abruptly changed. As shown in Fig. 1a, the intensity profile indicates that the cubic phase in the above compounds disappeared in the $Sb_{52}Te_{48}$ compound. Partial $Sb_{52}Te_{48}$ began to directly crystallize to the trigonal phase at 120 °C (Supplementary Fig. 3). With increasing temperature, additional crystalline diffraction spots appeared. Up to 160 °C, the compound completely crystallized to the trigonal phase. In comparison, when the composition of the Sb–Te compound approached Sb_2Te, all the compounds quickly crystallized into the trigonal phase at 140 °C (Supplementary Fig. 4).

According to the results of the in situ heating experiments, the phase transition temperatures vs various Sb concentrations are summarized in Fig. 1b. As shown in the figure, a distinct boundary appeared when the Sb concentration equaled 50%. When the Sb concentration was greater than 50%, the cubic phase was not observed. The cubic phase was only obtained when the Sb concentration was lower than 50%. In addition, the data reveal that the phase transition temperatures of both the amorphous-cubic and cubic-trigonal phases increased with increasing Sb concentration or decreasing amount of vacancies of the Sb sites in the cubic Sb–Te compounds.

Ab initio calculations revealing the stability of FCC Sb–Te structures with different types and amounts of vacancies

To understand the in situ heating TEM experimental results, we performed ab initio calculations. For a comparison with the trigonal phase, a hexagonal supercell with P1 symmetry was designed according to the FCC structure, with 108 Sb atoms on one sublattice and 108 Te atoms on the other sublattice. Based on this structure, Sb and Te atoms were removed randomly to create vacancies, and then the structures were relaxed to their ground state energy. By removing 36 Sb atoms, the composition of the supercell was the same as Sb_2Te_3. By removing 54 Te atoms, the composition of the supercell was the same as Sb_2Te.

As presented by the atomic models in Fig. 2a, the structural frameworks of the cubic phase remained well defined after removing the Sb atoms, even when the number of atoms removed reached 36. In contrast, the removal of 18 Te atoms severely deformed the local structures. After removing 36 Te atoms, the framework of the cubic structure was completely destroyed, and the situation deteriorated after removing 54 Te atoms. In addition, the corresponding formation energy (E_f) was also calculated to reveal the stability of the cubic structures.

As depicted in Fig. 2b, the cubic structure with Sb vacancies had a negative E_f. The value of E_f was the lowest
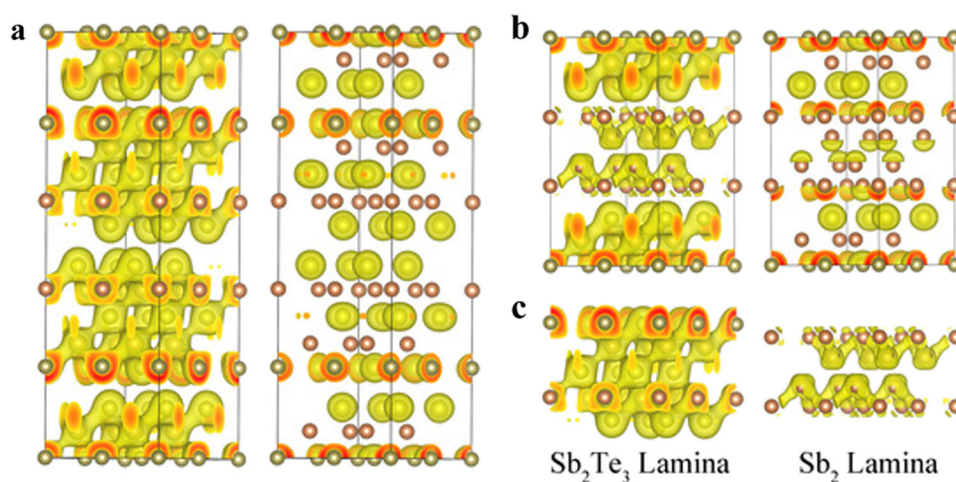
Fig. 3 The charge denstiy maps showing the bonding and antibonding states of stable trigonal Sb_2Te_3 and Sb_2Te phases. a, b Charge density maps of the bonding states and antibonding states for trigonal Sb_2Te_3 and Sb_2Te. **c** Sb_2Te_3 and Sb_2 lamina extracted from the Sb_2Te_3 and Sb_2Te trigonal phases. The bonding and antibonding energy ranges were selected from the COHPs in Supplementary Fig. 6. For trigonal Sb_2Te_3, the energy window for the charge density map of the antibonding states was −1.95 ~ 0 eV, and the energy window of the bonding states was −5.87 to approximately −2.00 eV. For trigonal Sb_2Te, the corresponding energy windows were −2.30 to ~0 eV and −6.07 to ~−2.36 eV, respectively. The iso-surfaces for the antibonding states were set to 60% of the maximum point, and those for the bonding states were set to 50% of the maximum point
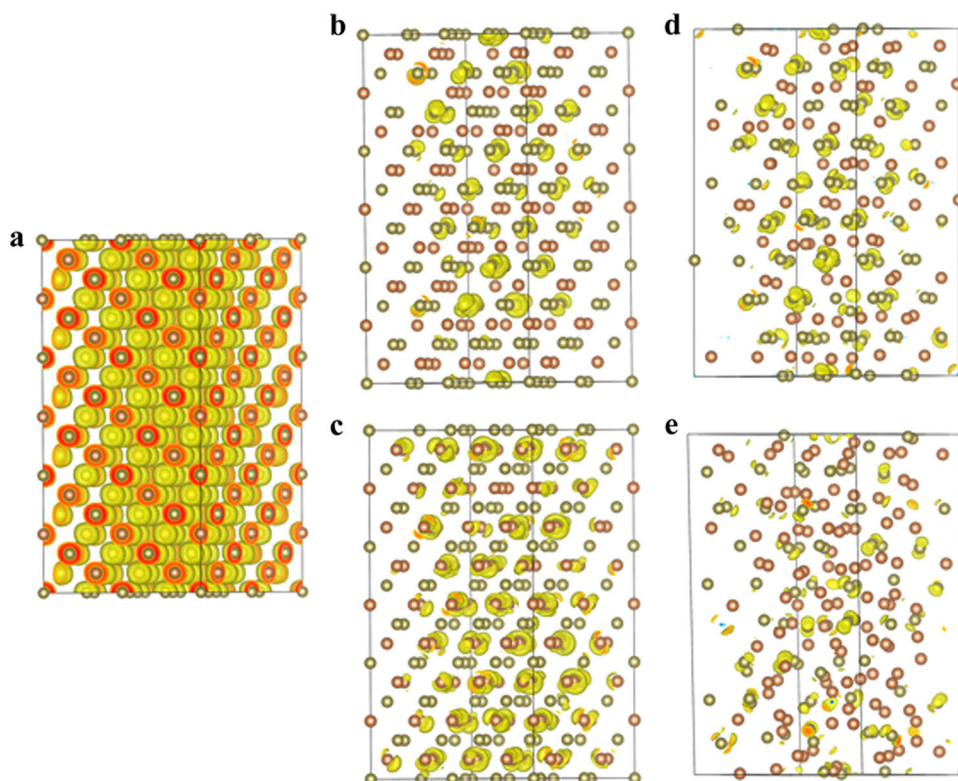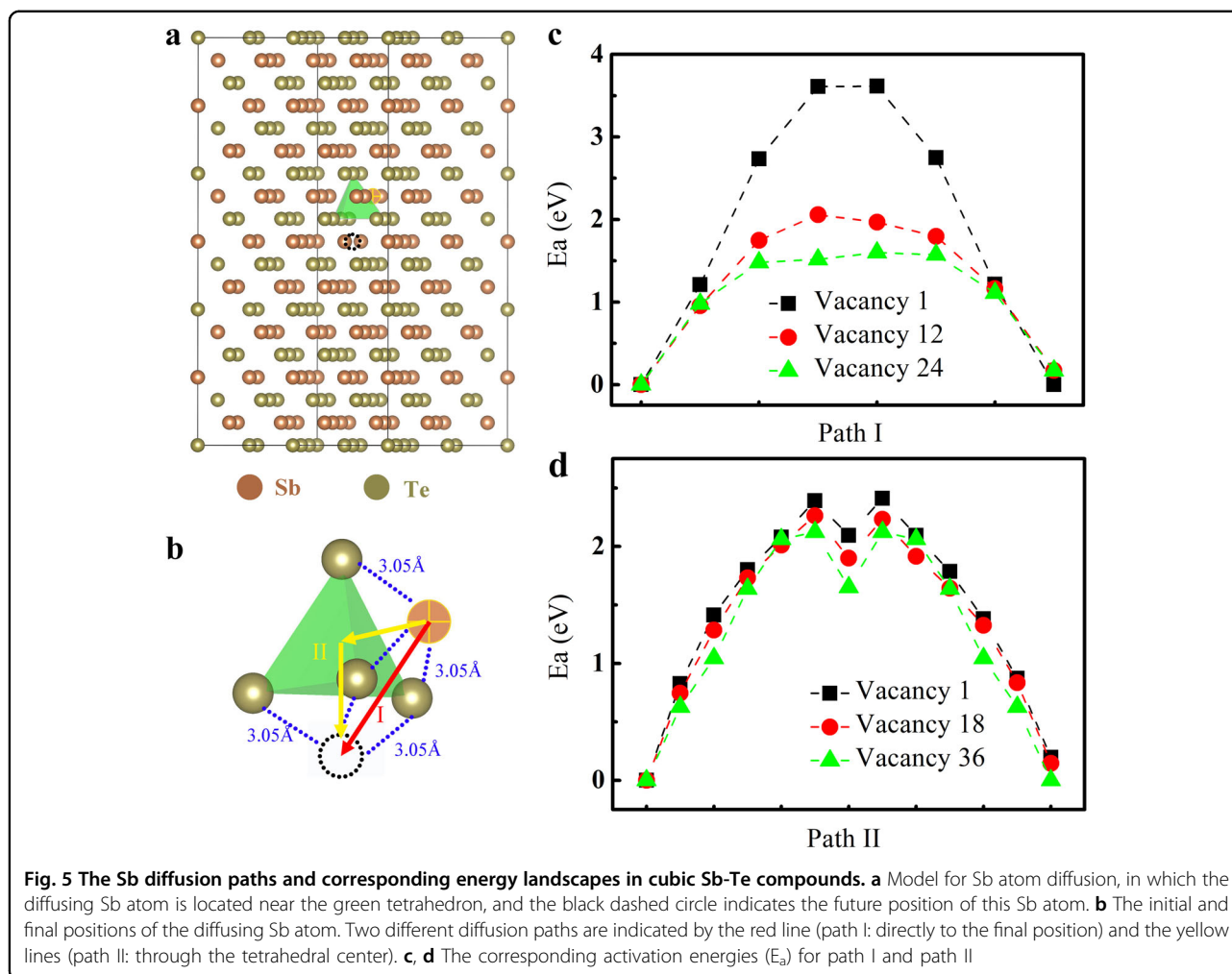
Fig. 4 Charge density maps of the antibonding states for the theoretical FCC structure of a $Sb_{108}Te_{108}$, b $Sb_{72}Te_{108}$ and c $Sb_{108}Te_{72}$ and the corresponding relaxed structures of d $Sb_{72}Te_{108}$ and e $Sb_{108}Te_{72}$. The antibonding energy ranges were selected from the COHP in Supplementary Fig. 7. The energy window for $Sb_{108}Te_{108}$ was $-2.5 \sim 0$ eV. The energy window for both the relaxed and unrelaxed structures of $Sb_{72}Te_{108}$ was $-1.9 \sim 0$ eV. The energy windows for the relaxed and unrelaxed structures of $Sb_{108}Te_{72}$ were $-1.8 \sim 0$ eV and $-2.4 \sim 0$ eV, respectively. The iso-surfaces are set to 60% of the maximum point

when the composition approached $Sb_{72}Te_{108}$ (namely, Sb_2Te_3), and E_f gradually increased to zero as the Sb concentration approached 50%. The low value of E_f means that Sb_2Te_3 was more energetically favorable. This explains why the as-deposited Sb_2Te_3 crystallized at room temperature. When the Sb concentration was above 50%, E_f increased above zero except for in $Sb_{108}Te_{90}$. Even with a negative formation energy, the cubic structure was impossible because of the severe deformation of the structural framework, as shown in Fig. 2a.

Charge density maps revealing the electronic structures of the Sb–Te phase

To understand what leads to the distinct behaviors of the phase transition for Sb–Te compounds, we revisit the basic electronic structure of Sb and Te atoms, which have s^2p^3 and s^2p^4 outer shell structures, respectively. Therefore, the most favorable bonding environments for Sb and Te are 3 and 2 p-bonding coordinated atoms, respectively. Figure 3a and b shows the charge density maps of the stable phases for Sb_2Te_3 and Sb_2Te, respectively.

As shown in the left panel in Fig. 3a, the most stable compound for Sb–Te alloys was the Sb_2Te_3 trigonal phase, where, on average, Sb has 3 coordinated Te atoms and Te has 2 coordinated Sb atoms. Even for the stable phase, the local coordination environments for Sb and Te were not perfect. Thus, antibonding states still existed in the stable phase (Supplementary Fig. 6, the crystal orbital Hamilton populations (COHPs) of Sb_2Te_3 and Sb_2Te). As shown in the right panel in Fig. 3a, these antibonding states were dominated by electrons surrounding Te. Moreover, in the octahedral bonding environment, Te–Te bonding was not favorable because the coordination environment was contradictory to the preferable requirement, which is the right angle zigzag chain structure[31]. In contrast, Sb–Sb bonding was more energetically preferable than Te–Te bonding because the bonds can be saturated with three perpendicular p-bonds, as shown by the Sb_2 lamina in Fig. 3c. For the Sb_2Te compound, the most stable structure was constructed by one laminar Sb_2Te_3 layer plus two extra laminar Sb_2 layers (Fig. 3b). These basic facts set up the prerequisites that the alloying structures must obey in the phase transitions.

Fig. 5 The Sb diffusion paths and corresponding energy landscapes in cubic Sb-Te compounds. a Model for Sb atom diffusion, in which the diffusing Sb atom is located near the green tetrahedron, and the black dashed circle indicates the future position of this Sb atom. **b** The initial and final positions of the diffusing Sb atom. Two different diffusion paths are indicated by the red line (path I: directly to the final position) and the yellow lines (path II: through the tetrahedral center). **c, d** The corresponding activation energies (E_a) for path I and path II

When Sb and Te were arranged into a theoretical rock-salt (RS) structure, there were 7 electrons in the Sb and Te p-orbitals. This means that the p-orbitals for Sb and Te were overloaded. Thus, the extra electrons in the p-orbitals were forced into the antibonding states. In this RS structure, as shown in Fig. 4a, the electrons of the anti-bonding states (Supplementary Fig. 7a) surrounded both Sb and Te atoms, and the energy of the Sb–Te composite was high. Removing Sb atoms decreased the formation energy of the cubic Sb–Te composites, as shown in Fig. 2b. In contrast, vacancies of the Te sites greatly increased the formation energy of the Sb–Te compounds and destroyed the cubic framework. Figure 4b, c show the charge density maps of the antibonding states for unrelaxed cubic $Sb_{72}Te_{108}$ and $Sb_{108}Te_{72}$, respectively. As shown in Fig. 4b, after removing 36 Sb atoms, the electrons of the anti-bonding states were only found around the Te atoms. This is similar to the charge density map of the antibonding states for trigonal Sb_2Te_3, indicating a decreased forma-tion energy. However, the vacancies of the Te sites

resulted in more antibonding electrons (Supplementary Fig. 7b and c). Furthermore, in contrast to $Sb_{72}Te_{108}$, the antibonding electrons in $Sb_{108}Te_{72}$ mainly surrounded the Sb atoms, suggesting a relatively high formation energy.

Relaxation further deceased the ground state of a structure by finding more suitable atom positions in a cell. As shown in Fig. 4d, the structure of $Sb_{72}Te_{108}$ adjusted slightly due to the similarity of the distributions of the antibonding electrons between cubic and trigonal phases. In contrast, the dramatic difference in the distribution of antibonding electrons in the $Sb_{108}Te_{72}$ composite resulted in a high driving force for the relaxation of the structure (this can also be seen from the COHP difference before and after the relaxation in Supplementary Fig. 7c and d). This difference collapsed the cubic framework. The charge density map in Fig. 4e shows that the atoms sur-rounded by antibonding electrons changed to Te from Sb after relaxation. Some Sb–Sb bonds appeared after relaxation (Supplementary Fig. 8). These results agree well with the structure of trigonal Sb_2Te.

Vacancies decreasing the diffusion energy barriers

The phase transition temperature from the cubic phase to the trigonal phase was determined by the activation energy (E_a) for atom/vacancy diffusion in the cubic framework. The activation of diffusion is required by the vacancy ordering and evaporation in the phase transition. This activation energy is defined by the energy barrier that the atom/vacancy must overcome in the diffusion path. Figure 5a shows a model for Sb atom diffusion. The diffusing Sb atom was situated near the green tetrahedron in Fig. 5a, and the black dashed circle indicates the future position of this Sb atom. In Fig. 5b, the initial and final positions for this Sb atom are clearly presented. Two different diffusion paths are also shown, where the red arrow indicates path I (directly to the final position) and the yellow arrow indicates path II (through the tetrahedral center). In the case of decreased vacancies (vacancy 1), the activation energy (E_a) required for the Sb atom to cross the energy barrier in path II was obviously lower than that in path I, as shown by Fig. 5c, d, respectively. With an increase in the number of vacancies, E_a shows a sharper decrease for path I than for path II. Although the number of vacancies had a different impact on E_a for path I and path II, E_a decreased as the number of vacancies increased in both cases. More vacancies means a large space to relax in during the atom diffusion process, which decreased the energy barriers that must be overcome by the diffusing atoms. This agrees well with our experimental results and the corresponding phenomenon in GeTe-Sb_2Te_3 pseudobinary alloys, where more Sb_2Te_3 means a decreased phase transition temperature[9].

The metastable cubic phases in our in situ TEM experiments only appeared when the Sb concentration was lower than 50%. This special composition-dependent phase transition was also demonstrated in thick samples (~100 nm) by resistance-temperature (R-T) measurements (Supplementary Fig. 9).

In summary, in situ heating TEM experiments combined with ab initial calculations were employed to understand the phase transitions in Sb–Te binary compounds. Vacancies were found to have a strong impact on the stability of cubic phases for Sb–Te compounds. The distribution of antibonding electrons supplied the driving force for the structural transitions. Furthermore, the results also showed that reducing the vacancies greatly increased the phase transition temperatures for both amorphous-cubic and cubic-trigonal phases, thus improving the data retention ability and cyclability. Doping may reduce the vacancies of the crystalline phase. Moreover, this also increased the stability of the amorphous phase[9], further improving the data retention ability. Doping Sb–Te compounds may provide an approach to discover better phase change materials for DRAM applications.

Author details
[1]State Key Laboratory of Functional Materials for Informatics, Shanghai Institute of Micro-system and Information Technology, Chinese Academy of Sciences, 200050 Shanghai, China. [2]Institute of Microstructure and Property of Advanced Materials, Beijing University of Technology, 100124 Beijing, China. [3]School of Physical Science and Technology, Shanghai Tech University, 201210 Shanghai, China. [4]Key Laboratory of Polar Materials and Devices (MOE), Department of Optoelectronics, East China Normal University, 200241 Shanghai, China

Author contributions
X.C. performed the in situ TEM observation and ab initio calculations. Y.C. designed the in situ heating TEM experiments. X.C. and X.L. analyzed the experimental and theoretical results. X.L. and X.C. wrote the paper with the help from all coauthors. The project was initiated and conceptualized by X.L. and Z.S.

Conflict of interest
The authors declare that they have no conflict of interest.

Publisher's note
Springer Nature remains neutral with regard to jurisdictional claims in published maps and institutional affiliations.

Supplementary information is available for this paper at https://doi.org/10.1038/s41427-019-0140-z.

References
1. Sarwat, S. G. et al. Scaling limits of graphene nanoelectrodes. *Nano Lett.* **17**, 3688–3693 (2017).
2. Sarwat, S. G. Materials science and engineering of phase change random access memory. *Mater. Sci. Technol.* **33**, 1890–1906 (2017).
3. Wong, H. S. P. & Salahuddin, S. Memory leads the way to better computing. *Nat. Nanotechnol.* **10**, 191 (2015).
4. Raoux, S., Xiong, F., Wuttig, M. & Pop, E. Phase change materials and phase change memory. *MRS Bull.* **39**, 703–710 (2014).
5. Burr, G. W. et al. Phase change memory technology. *J. Vac. Sci. Technol.* **28**, 223–262 (2010).
6. Wuttig, M. & Yamada, N. Phase-change materials for rewriteable data storage. *Nat. Mater.* **6**, 824–832 (2007).
7. Rao, F. et al. Reducing the stochasticity of crystal nucleation to enable sub-nanosecond memory writing. *Science* **1427**, 1–9 (2017).
8. Zheng, Y. et al. Direct observation of metastable face-centered cubic Sb_2Te_3 crystal. *Nano Res.* **9**, 3453–3462 (2016).
9. Wuttig, M. et al. The role of vacancies and local distortions in the design of new phase-change materials. *Nat. Mater.* **6**, 122–128 (2007).
10. Liu, X. Q. et al. New structural picture of the $Ge_2Sb_2Te_5$ phase-change alloy. *Phys. Rev. Lett.* **106**, 025501 (2011).
11. Kolobov, A. V., Fons, P., Tominaga, J. & Ovshinsky, S. R. Vacancy-mediated three-center four-electron bonds in GeTe-Sb2Te3 phase-change memory alloys. *Phys. Rev. B: Condens. Matter Mater. Phys.* **87**, 1–9 (2013).
12. Siegrist, T. et al. Disorder-induced localization in crystalline phase-change materials. *Nat. mater.* **10**, 202–208 (2011).
13. Zhang, W. et al. Role of vacancies in metal-insulator transitions of crystalline phase-change materials. *Nat. Mater.* **11**, 952–956 (2012).
14. Bragaglia, V. et al. Metal - Insulator Transition Driven by Vacancy Ordering in GeSbTe Phase Change Materials. *Sci. Rep.* **6**, 23843 (2016).
15. Siegert, K. S. et al. Impact of vacancy ordering on thermal transport in crystalline phase-change materials. *Rep. Prog. Phys.* **78**, 013001 (2015).

16. Behrens, M. et al. Impact of disorder on optical reflectivity contrast of epitaxial Ge$_2$Sb$_2$Te$_5$ thin films. *Crystengcomm* **20**, 3688 (2018).

17. Duck, M. M. et al. Disorder control in crystalline GeSb$_2$Te$_4$ and its impact on characteristic length scales. *Rapid Res. Lett.* **13**, 1800578 (2019).

18. Kim, I. S. et al. High performance PRAM cell scalable to sub-20nm technology with below 4F^2 cell size, extendable to DRAM applications. in Digest of Technical Papers - Symposium on VLSI Technology 203–204 (2010).

19. Zhu, M. et al. One order of magnitude faster phase change at reduced power in Ti-Sb-Te. *Nat. Commun.* **5**, 1–6 (2014).

20. Ding, K. et al. The impact of W doping on the phase change behavior of Sb$_2$Te$_3$. *J. Alloy. Compd.* **688**, 22–26 (2016).

21. Njoroge, W. K., Wöltgens, H.-W. & Wuttig, M. Density changes upon crystallization of Ge$_2$Sb$_{2.04}$Te$_{4.74}$ films. *J. Vac. Sci. Technol.* **A 20**, 230–233 (2002).

22. Kresse, G. & Furthmüller, J. Efficiency of ab-initio total energy calculations for metals and semiconductors using a plane-wave basis set. *Comput. Mater. Sci.* **6**, 15–50 (1996).

23. Joubert, D. From ultrasoft pseudopotentials to the projector augmented-wave method. *Phys. Rev. B: Condens. Matter Mater. Phys.* **59**, 1758 (1999).

24. Perdew, J. P., Burke, K. & Ernzerhof, M. Generalized gradient approximation made simple. *Phys. Rev. Lett.* **77**, 3865–3868 (1996).

25. Grimme, S. Semiempirical GGA-type density functional constructed with a long-range dispersion correction. *J. Comput. Chem.* **27**, 1787–1799 (2006).

26. Dronskowski, R. & Blöchl, P. E. Crystal orbital Hamilton populations (COHP): Energy-resolved visualization of chemical bonding in solids based on density-functional calculations. *J. Phys. Chem.* **97**, 8617–8624 (1993).

27. Maintz, S., Deringer, V. L., Tchougreeff, A. L. & Dronskowski, R. LOBSTER: A tool to extract chemical bonding from plane-wave based DFT. *J. Comput. Chem.* **37**, 1030–1035 (2016).

28. Deringer, V. L., Tchougréeff, A. L. & Dronskowski, R. Crystal orbital Hamilton population (COHP) analysis as projected from plane-wave basis sets. *J. Phys. Chem. A* **115**, 5461–5466 (2011).

29. Henkelman, G., Uberuaga, B. P. & Jónsson, H. Climbing image nudged elastic band method for finding saddle points and minimum energy paths. *J. Chem. Phys.* **113**, 9901–9904 (2000).

30. Henkelman, G. & Jónsson, H. Improved tangent estimate in the nudged elastic band method for finding minimum energy paths and saddle points. *J. Chem. Phys.* **113**, 9978–9985 (2000).

31. Gaspard, J. P., Pellegatti, A., Marinelli, F. & Bichara, C. Peierls instabilities in covalent structures I. Electronic structure, cohesion and the $Z = 8 - N$ rule. *Philos. Mag. B* **77**, 727–744 (1998).